

Special Section:

Fifteen Years of THEMIS Mission

Key Points:

- We utilize the oxygen Auger electron peak to isolate cases of emitted electrons dominated by backscattered electrons (BSE) over photoelectrons
- We derive the electron backscattering coefficient η of the lunar surface to be 0.1–0.3 for 50–600 eV
- We reveal η to be dependent on the magnetic dip angle, as some BSE re-impact the surface in a magnetized environment

Supporting Information:

Supporting Information may be found in the online version of this article.







Correspondence to:S. Xu,
shaosui.xu@ssl.berkeley.edu**Citation:**

Xu, S., Poppe, A. R., Szabo, P. S., Harada, Y., Halekas, J. S., & Chamberlin, P. C. (2023). Characteristics of lunar surface electrons inferred from ARTEMIS observations: 1. Backscattered electrons. *Journal of Geophysical Research: Planets*, 128, e2023JE007983. <https://doi.org/10.1029/2023JE007983>

Received 3 JUL 2023

Accepted 5 OCT 2023

Characteristics of Lunar Surface Electrons Inferred From ARTEMIS Observations: 1. Backscattered Electrons

Shaosui Xu¹ , Andrew R. Poppe¹ , Paul S. Szabo¹ , Yuki Harada² , Jasper S. Halekas³ , and Phillip C. Chamberlin⁴ 

¹Space Sciences Laboratory, University of California, Berkeley, Berkeley, CA, USA, ²Department of Geophysics, Kyoto University, Kyoto, Japan, ³Department of Physics and Astronomy, University of Iowa, Iowa City, IA, USA, ⁴Laboratory for Atmospheric and Space Physics, University of Colorado Boulder, Boulder, CO, USA

Abstract Lunar surface charging is a scientifically and practically important topic at the Moon that is largely determined by the electron currents near the surface. Among those electron populations, lunar photoelectrons (PHE) and backscattered electrons (BSE) produced by incident electrons that make up the high-energy tail of lunar emitted electrons are not well characterized yet. Recently, Xu et al. (2021, <https://doi.org/10.1029/2020je006790>) reported oxygen Auger electron observations at the Moon by the Acceleration, Reconnection, Turbulence, and Electrodynamics of the Moon's Interaction with the Sun spacecraft, which provides a unique feature to identify lunar photoelectrons. We utilize this feature to isolate cases of emitted electrons dominated by BSE over PHE. With selected BSE cases, we characterize how the backscattering coefficient η varies with primary electron energy, which decreases with increasing energy. Our results also reveal η to be dependent on the magnetic dip angle, as a fraction of BSE re-impact the surface in a magnetized environment. The characterization of the backscattering coefficient not only gives insights into the lunar surface properties and lunar surface charging but could also be potentially applied to other airless bodies.

Plain Language Summary Lunar surface is electrically charged to different degrees depending on the space environment of the Moon. Lunar surface charging is an important topic for robotic and human lunar exploration, as well as scientific observations from the surface. One of the quantities related to the lunar surface charging is the backscattering coefficient, which represents the probability that an incident electron is backscattered away from the lunar surface after impact as opposed to be absorbed by the surface. This study provides estimates of the electron backscattering probability with measurements from the Acceleration, Reconnection, Turbulence, and Electrodynamics of the Moon's Interaction with the Sun spacecraft. We have determined the probability to be 0.1–0.3 at different electron energies. This is also affected by the magnetized environment at the Moon, causing some initially scattered electrons to return to the surface. The characterization of the backscattering coefficient not only gives insights into lunar surface charging and the lunar surface properties but could also be potentially applied to other airless bodies.

1. Introduction

Surface charging in space, a fundamental physical process, is determined by the ambient currents near the surface and the surface properties, giving rise to a floating potential with respect to the surrounding plasma such that the net current is zero (Whipple, 1981). The lunar surface is electrically charged to different degrees depending on the photon and the ambient plasma environment (Kallio et al., 2012; Nitter et al., 1998). Lunar surface charging is both scientifically and practically important. Near-surface electric fields arising from lunar surface charging significantly affect the plasma environment near the surface. High surface potential could potentially lead to dynamic charged dust transport (A. Poppe & Horányi, 2010; Schwan et al., 2017; Sternovsky et al., 2008; Wang et al., 2016) and modify exospheric pickup ion dynamics (A. Poppe et al., 2013). Electric fields and dust near the surface may have important practical implications for robotic and human lunar exploration, as well as scientific observations from the surface (Farrell et al., 2008).

Lunar surface charging is typically dominated by currents from the lighter and faster electrons over those due to ions. Near the lunar surface, the main electron populations are: (a) incident ambient electrons that are of solar wind and/or terrestrial magnetospheric origin; (b) secondary and backscattered electrons (BSE) produced by incident electrons interacting with the surface (e.g., Halekas et al., 2009a; Manka, 1973); and (c) photoelectrons

produced by the solar photons ionizing the lunar surface (e.g., Halekas et al., 2012b; Kato et al., 2023; A. Poppe et al., 2012; Xu et al., 2021; Yokota et al., 2009). Note that, conventionally, secondary electrons are defined as the cold population less than 50 eV, and the BSE as the high energy tail of electrons emitted from the surface (e.g., Schreiber & Fitting, 2002; Thomas & Pattinson, 1970). However, there exists a more fundamental physical difference between the two, in that secondary electrons are electrons liberated from the surface by the incident electrons, while BSE are a fraction of the incident electrons that are reflected back to space. Depending on the specific environment, the lunar surface is typically positively charged in the sunlit hemisphere, from $< \sim 10$ V in the solar wind (e.g., Borovsky & Delzanno, 2021; Halekas et al., 2008, 2011b) to tens to hundreds of volts in the magnetotail lobes (Harada et al., 2013, 2017; Pedersen, 1995), and negatively charged in darkness, up to negative hundreds of volts (Halekas et al., 2002, 2008, 2011b) or sometimes kilovolts during solar energetic particle events (Halekas et al., 2007, 2009b). Inside Earth's magnetotail plasma sheet, non-monotonic sheath potentials can occur above the dayside surface (Collier et al., 2017; Halekas et al., 2011a; A. Poppe et al., 2011; A. R. Poppe et al., 2012).

Among electron populations that are emitted from the lunar surface, secondary electrons have been well characterized by previous studies (e.g., Halekas et al., 2009a) but the BSE and photoelectrons that make up the high-energy tail have been less well characterized. Recently, Xu et al. (2021) reported oxygen Auger electron observations at the Moon by the Acceleration, Reconnection, Turbulence, and Electrodynamics of the Moon's Interaction with the Sun (ARTEMIS) spacecraft, reproduced in the modeling effort by Kato et al. (2023), which provides a unique feature to identify lunar photoelectrons (PHE). Thus, this spectral feature can be used to separate photoelectrons from the BSE. In this study, we focus on the characterization of the BSE with ARTEMIS observations, more specifically the backscattering coefficient, that is, the probability that a single incident electron is backscattered to space as opposed to being absorbed by the surface. The backscattering coefficient is also one of the fundamental properties of a solid surface, which has not been well characterized for the lunar surface yet. To investigate the electron backscattering from the Moon, we consider ARTEMIS observations when the Moon is immersed in the upstream solar wind, where the BSE produced by the incident solar wind electrons are often intense enough to dominate over lunar photoelectrons that escape the near-surface sheath and travel up to the ARTEMIS spacecraft. This paper is organized as follows: Section 2 describes the instruments, data selection, and method to derive the backscattering coefficient with ARTEMIS observations; Section 3 presents relevant results on the derived backscattering coefficients together with a sensitivity study; we then discuss the results and conclude the study in Section 4.

2. Methodology

In this section, we introduce the data selection and the method to derive the backscattering coefficient, $\eta(E_p)$, where E_p is the primary electron energy. Data used in this study are from the ARTEMIS mission, which consists of two probes orbiting near the Moon's equator in elliptical orbits, P1 and P2 (originally probes B and C of the Time History of Events and Macroscale Interactions during Substorms mission) (Angelopoulos, 2009). Each probe carries a comprehensive suite of plasma and field instruments (Angelopoulos, 2011) and has been collecting data in the lunar plasma environment since mid-2011. Relevant data are sub-keV electron observations from the Electro-Static Analyzer (ESA) (McFadden et al., 2008) and magnetic field vectors measured by the fluxgate magnetometer (FGM) (Auster et al., 2008) from both probes from 2011 to 2020. To properly resolve and utilize the oxygen Auger electron peak in the photoelectron energy spectrum, the burst electron data product is used, which provides the highest energy, angle, and time resolution (32 energies by 88 angles at ~ 4 s time resolution) available. The spacecraft potential measured by the Electric Field Instrument (EFI), publicly available as part of the standard data products (Bonnell et al., 2009), is used to correct the measured electron fluxes.

This study focuses on times when the Moon is immersed in the solar wind, as determined by selecting data when ARTEMIS is outside of an empirical Earth bow shock, following Xu et al. (2019, 2020). To investigate electrons emitted from the lunar dayside surface, we select cases when the measured magnetic field is connected to the lunar surface (using a straight-line approximation) and the contact point is located at a solar zenith angle (SZA) $< 90^\circ$. A maximum spacecraft altitude of 1,500 km is imposed to enhance the accuracy of the straight-line approximation. We additionally require the spacecraft to be at SZA $< 85^\circ$ to avoid any complications in interpreting the data near the lunar terminator. As electrons are magnetically reflected outside of the loss cone pitch angles (PAs) before impacting the surface, we require the ratio of the measured magnetic strength at the

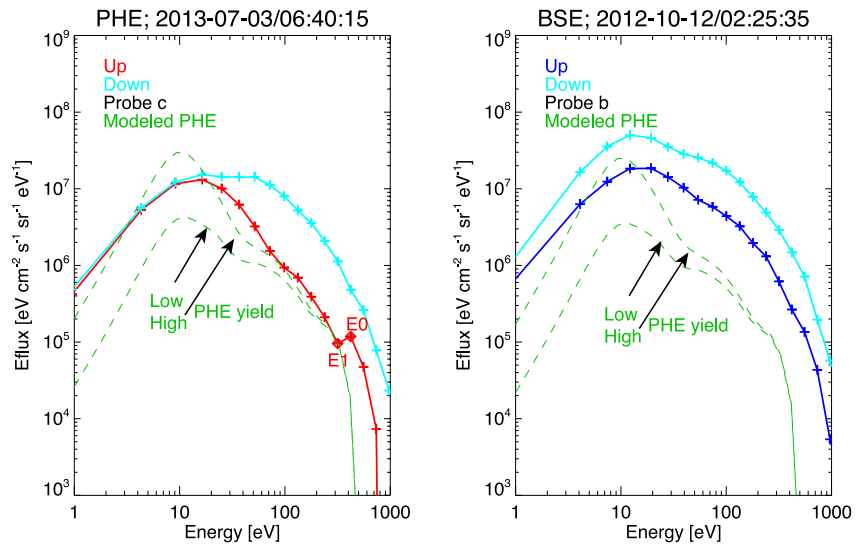


Figure 1. Two examples of electron energy spectra measured by ARTEMIS when the Moon is in the solar wind, at times indicated in the figure titles. Both cases have solar wind electrons (cyan) traveling toward the Moon but different upward electron populations, dominated by photoelectrons (left, red) and backscattered electrons (right, blue), respectively. The highlighted E0 and E1 in the left panel are the two adjacent energy channels used to identify the oxygen Auger electron peak. All the electron fluxes have been corrected for spacecraft potentials. The two dashed green lines are the modeled photoelectron energy spectra using the solar irradiance spectra from FISM2 and the low and high photoemission yields adopted from Xu et al. (2021), their Figure 7.

spacecraft and the surface crustal field strength (estimated from a crustal model (Mitchell et al., 2008)) to be larger than 1. To minimize the impact of magnetically reflected electrons and to pick out pure BSE emitted from the surface, we further confine our search to a geographic box where the crustal magnetic fields are minimized, longitude = [210°, 300°] and latitude = [−10°, 10°] (Halekas et al., 2012a; Jarvinen et al., 2014). Finally, we can determine down-precipitating and upgoing electrons, from which to obtain primary electrons and BSE, by combining the pitch angle and the angle between the magnetic field and the surface normal vector (or the magnetic dip angle α_{Bn}).

2.1. Selection of BSE Events

The high-energy (>50 eV) tail of outgoing electrons from the lunar surface can be dominated by either PHE or BSE depending on their relative fluxes. Figure 1 illustrates two examples where the dominant upcoming electrons are PHE (red line in the left panel) and BSE (blue line in the right panel), respectively, with comparison to the downward-precipitating solar wind electrons (SWE; cyan lines in both panels). Both cases have been corrected for spacecraft potentials. A few observations can be made from Figure 1: (a) the BSE energy spectrum resembles the downward-precipitating SWE energy spectrum with much lower fluxes (right panel); (b) the shape of the PHE energy spectrum is distinctively different from SWE, with comparable fluxes below ~30 eV and a relative deficit of flux >30 eV; and (c) a flux peak can be identified in the energy spectrum at ~420 eV corresponding to the oxygen Auger electron peak (Xu et al., 2021), which is absent from the BSE case due to higher BSE flux. In particular, the Auger electron peak is unique to PHE and can be utilized to separate these two populations, which can be identified by comparing the fluxes of E0 (the closest energy channel to ~420 eV) and E1, as indicated in the left panel. We define a quantity $S = \frac{\ln(f_{E0}) - \ln(f_{E1})}{\ln(E0) - \ln(E1)}$, which should be negative for BSE (e.g., $S = -3$ for the BSE flux in Figure 1) and positive for PHE (e.g., $S = 0.85$ for the PHE flux in Figure 1). Additionally, we can take advantage of another property of PHE, whose fluxes scale directly with solar EUV photon fluxes (Xu & Liemohn, 2015; Xu et al., 2015). It means photoelectron fluxes should vary by one to two orders of magnitude with solar cycle (except for intense flare events) (Sternovsky et al., 2008). Observationally, the Auger electron fluxes are on the order of 10^4 – 10^5 eV cm^{−2} s^{−1} sr^{−1} eV^{−1}.

Figure 2 shows a scatterplot of electron differential energy fluxes at E0 (f_{E0}) as a function of S for upward electron energy spectra satisfying the aforementioned selection criteria, with the two example cases shown in Figure 1

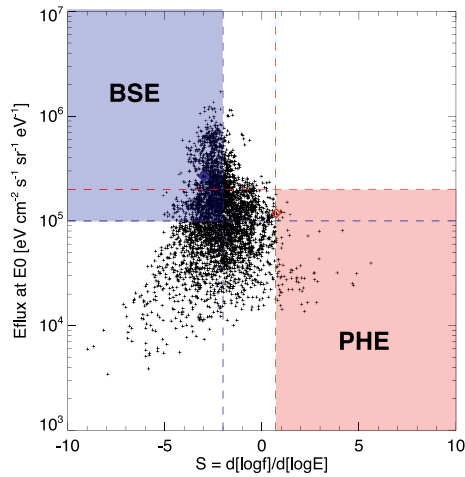


Figure 2. A scatterplot of electron differential energy fluxes at E0 (f_{E0}) against energy flux gradient $S = \frac{\ln(f_{E0}) - \ln(f_{E1})}{\ln(E0) - \ln(E1)}$ for selected upward electron energy spectra, where E0 and E1 are indicated in Figure 1. Those with $f_{E0} > 1 \times 10^5 \text{ eV cm}^{-2} \text{ s}^{-1} \text{ sr}^{-1} \text{ eV}^{-1}$ and $S < -2$ (the upper left quadrant highlighted by the two blue dashed lines) are cases dominated by backscattered electrons (BSE). Those with $f_{E0} < 2 \times 10^5 \text{ eV cm}^{-2} \text{ s}^{-1} \text{ sr}^{-1} \text{ eV}^{-1}$ and $S > 0.7$ (the lower right quadrant highlighted by the two red dashed lines) are cases dominated by photoelectrons (PHE). The two cases shown in Figure 1 are marked as red (PHE) and blue (BSE) diamonds, respectively.

marked as red (PHE) and blue (BSE) diamonds, respectively. Empirically, we find $S \geq 0.7$ is a satisfactory criterion to identify the Auger electron peak (thus indicating PHE) and $S \leq -2$ for BSE. Figure 2 suggests for $S \geq 0.7$, the Auger electron flux f_{E0} is $< 2 \times 10^5 \text{ eV cm}^{-2} \text{ s}^{-1} \text{ sr}^{-1} \text{ eV}^{-1}$. We thus impose a flux threshold of $f_{E0} > 1 \times 10^5 \text{ eV cm}^{-2} \text{ s}^{-1} \text{ sr}^{-1} \text{ eV}^{-1}$ for BSE, a slightly lower threshold to gain more data sampling. In short, our additional criteria to select BSE-dominant cases are $S \leq -2$ and $f_{E0} > 1 \times 10^5 \text{ eV cm}^{-2} \text{ s}^{-1} \text{ sr}^{-1} \text{ eV}^{-1}$, which results in 898 BSE cases (electron measurements).

Finally, as pointed out by Halekas et al. (2012a), the most useful frame for considering reflection from a moving obstacle is the de Hoffman-Teller (dHT) frame (De Hoffmann & Teller, 1950). In the dHT frame, any adiabatic reflection process perfectly conserves energy, with parallel velocities reversed and perpendicular velocities unchanged for reflecting particles. The transformation from the solar-wind frame to the dHT frame is performed via a transformation vector aligned with the IMF with a magnitude of $-\mathbf{v} \cdot \mathbf{n} / (\mathbf{B} \cdot \mathbf{n})$, where \mathbf{v} , \mathbf{B} , \mathbf{n} are the solar wind velocity, magnetic field, and surface normal vectors, respectively. All the selected cases have been transformed to the dHT frame accordingly for the following sections.

2.2. Integrated Primary Electron and BSE Spectra

Despite isolating ARTEMIS observations connected to weakly magnetized areas of the lunar surface, such weak crustal fields can nevertheless magnetically reflect a non-negligible portion of the down-going electrons. We thus need to determine whether upgoing electron fluxes stem from magnetic reflection or actual backscattering from lunar regolith grains. For our goal

of determining the backscattering coefficient $\eta(E_p)$, only the latter population is of interest. As illustrated in Figure 3, only down-going electrons within $180^\circ - LC < PA < 180^\circ$ can reach the surface without being magnetically reflected, where PA is short for pitch angle and LC for loss cone. At the lunar surface, Figure 3c, the

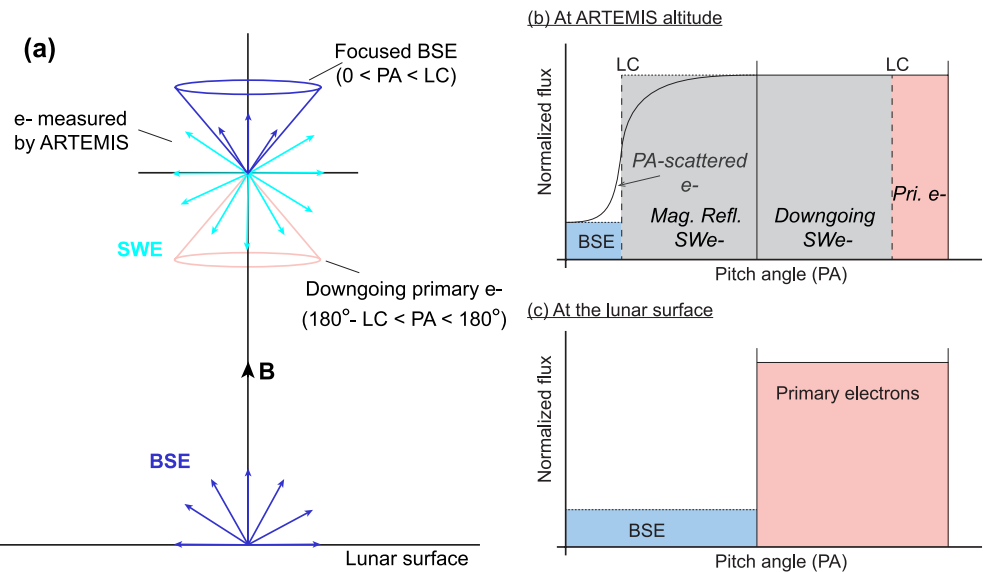


Figure 3. (a) A schematic shows down-going solar wind electrons (cyan) producing backscattered electrons (BSE) with a certain angular distribution (blue). Upward-going electrons measured by Acceleration, Reconnection, Turbulence, and Electrodynamics of the Moon's Interaction with the Sun (ARTEMIS) are a mixture of magnetically reflected or scattered electrons with more perpendicular pitch angles (cyan) and BSE in more field-aligned directions (blue). (b) Electron pitch angle distribution measured at ARTEMIS altitude with primary electrons within LC colored in pink, BSE in blue, down-going and magnetic reflected electrons outside of LC in gray. (c) Electron pitch angle distribution measured at the lunar surface, assuming an isotropic distribution for both primary electrons (pink) and BSE (blue).

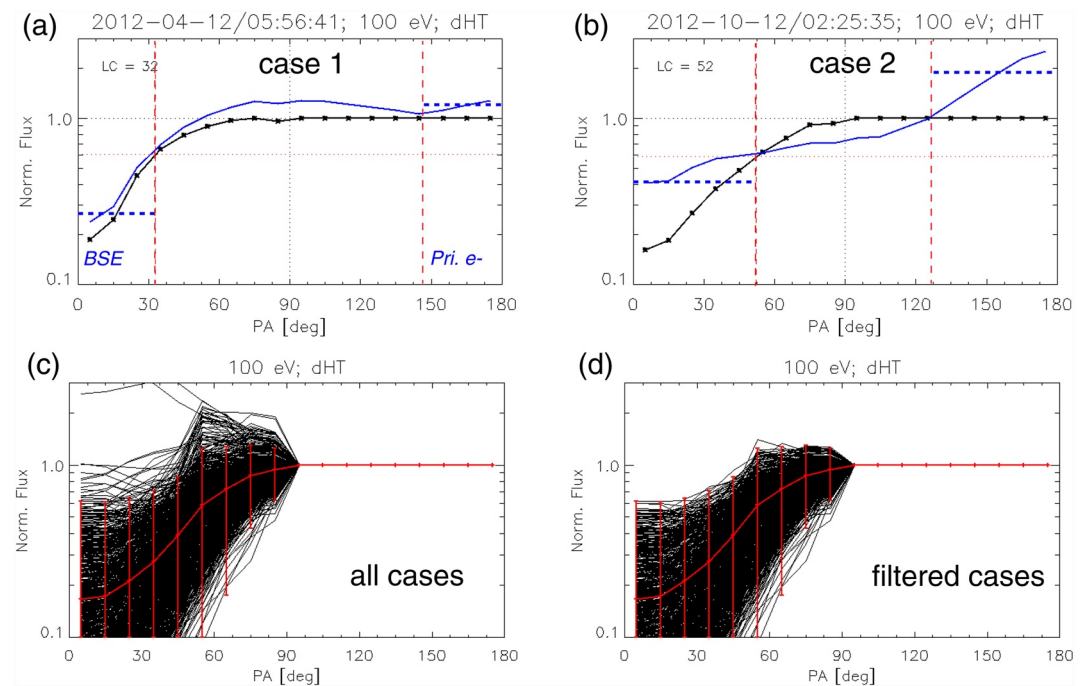


Figure 4. (a, b) Case studies of pitch angle (PA) distributions for determining the LC size at 100 eV. The PA is rearranged based on the measured magnetic vector such that PA 0°–90° are upgoing electrons and PA 90°–180° are down-going electrons. In both panels, the blue solid curves are measured electron fluxes divided by the averaged flux at 100 eV. For the black solid curve, upgoing electron fluxes at certain PAs are normalized to the corresponding down-going electron fluxes at supplementary PAs and thus down-going fluxes are all normalized to be 1. The red vertical dashed lines indicate the determined LC size and the two blue horizontal dashed lines are the determined BSE flux and primary electron flux. (c) The normalized PA distributions for all selected cases with the red curve showing the average values and the vertical lines are 2σ (standard deviation). (d) Filtered cases where the PA distributions are within 2σ .

primary solar wind electrons now fill all down-going PA and we furthermore assume that any BSEs are emitted isotropically. Correspondingly, BSE produced at the surface in all upward directions are then focused to upgoing electrons within $0 < PA < LC$ at the spacecraft altitude (Figures 3a and 3b). To derive the backscattering coefficient $\eta(E_p)$, we need to first determine the loss cone size for each measurement and then the integrated primary electron flux and BSE flux. Note also that wave-particle instabilities can scatter magnetically reflected upgoing electrons into the loss cone (Figure 3b) and thus, observed pitch-angle distributions do not generally have sharp boundaries but rather smoothed distributions as shown in Figure 3b.

Figure 4 illustrates two selected case studies for determining the LC size and normalized PA distributions. The PA is rearranged based on the measured magnetic vector such that PA 0°–90° are upgoing electrons and PA 90°–180° are down-going electrons. To obtain the LC size, we calculate the normalized PA distributions by dividing the flux of upgoing electrons at a certain PA of x by the corresponding down-going electron fluxes at PA of $180^\circ - x$, as shown as the black curves in all four panels. The LC size is determined to be the PA (the red vertical dashed line) at which the flux is the average of the minimum and maximum fluxes (equivalent of 50% depletion), as indicated by the red dotted horizontal lines. We then determine the primary electron flux to be the averaged flux within $180^\circ - LC < PA < 180^\circ$ and the BSE flux to be the minimum flux within $0 < PA < LC$ because the loss cone is partly filled by pitch angle scattered electrons. Panel c shows the normalized PA distributions for all selected cases, where we determine the averaged PA distribution shape and the 2σ (standard deviation). We then down-select cases with a 2σ requirement, as shown in Figure 4d, resulting in 828 “filtered” cases in total.

2.3. Removing PHE Contribution

The high-energy tail of electrons emitted from the lunar surface are always a mixture of backscattered and photo-emitted populations, their relative contribution depending on the solar irradiance and the solar wind

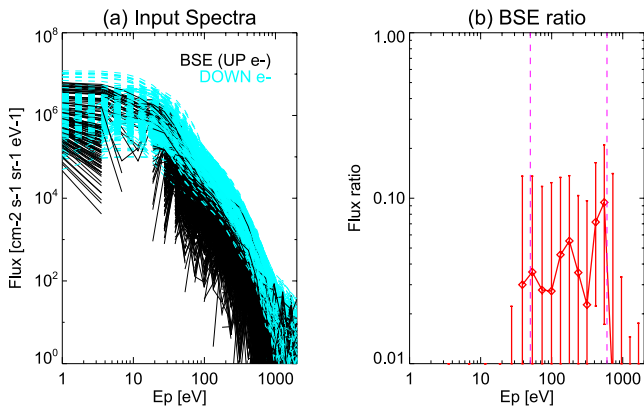


Figure 5. (a) Electron energy spectra for selected backscattered electrons (BSE) cases, cyan for downward primary electrons, and black for BSE corrected for photoelectrons contamination. (b) Median ratios of upward energy fluxes to downward energy fluxes as a function of electron energy for identified BSE cases, with the first and third quartiles as error bars.

electron flux. To remove the possible contamination of PHE in our selected BSE cases, we employ the methodology described by Xu et al. (2021) to model the PHE energy spectrum. More specifically, we use the solar irradiance spectra from Version 2 of the Flare Irradiance Spectral Model (FISM2) (Chamberlin et al., 2007, 2008, 2020), the probability function adopted from Feuerbacher et al. (1972), and also two photoemission yields shown in Figure 7 in Xu et al. (2021) (referred as “high” and “low” yields because of the uncertainty in surface potentials). The modeled photoelectron energy spectra are shown as the green dashed lines in Figure 1, lower and higher fluxes corresponding to low and high photoemission yields, respectively. By examining several case studies, the high-yield curve generally provides a better agreement with the upward electron fluxes for PHE-dominated cases at energies 30–400 eV, despite overestimating the PHE fluxes at <20–30 eV and underestimating Auger electron fluxes (both energy ranges are not well constrained by Xu et al. (2021)). Most recently (Kato et al., 2023) developed a numerical model of the energy spectrum of lunar photoelectrons and Auger electrons for the lunar environment, which is able to reproduce the observed oxygen Auger electron peak as a result of the solar photon flux. The main results of this study are using the high-yield correction and we will discuss the effects of this correction later.

Figure 5 shows the BSE (black) and primary electron (cyan) energy spectra for the selected 828 cases in the left panel and the ratio of the two fluxes in the right panel. The BSE energy spectra are the upward electron energy fluxes subtracted by the modeled PHE fluxes, missing data caused by overestimated PHE fluxes. The median flux ratio varies between a few percents to 10% within 40–600 eV. The sharp decrease in flux ratios above 600 eV is caused by electron fluxes approaching the instrument background flux level and we thus confine the energy range of interest to be 50–600 eV, excluding low energies dominated by secondary electrons, for the rest of the study. As it is complicated to reconstruct the angular distributions of primary electrons and BSE at the surface after magnetic focusing/reflection, we remove the angular dependence for deriving the backscattering coefficient by using the integrated fluxes of both populations, that is, the averaged fluxes shown in Figure 5a are multiplied by 2π .

2.4. Solving for the Backscattering Coefficient η

Observations (Vorburger et al., 2013) and modeling (Szabo et al., 2022) show that the surface structure of the regolith changes the angular dependence of the backscattering coefficient of protons from strongly increasing for oblique incidence to basically constant for all angles of incidence. As the angular dependence of the electron and proton backscattering for an idealized flat surface is similar, we can assume that the electron backscattering coefficient from regolith similarly becomes independent of the incidence angle. By integrating out the angular distributions of both the primary electrons and BSE, the theoretical derivation of the backscattering coefficient η is largely simplified and contains no angular information. Theoretically, the backscattered electron number flux, $jj(\epsilon)$, produced by primary electrons with a number flux, $j(E_p)$, is given by,

$$jj(\epsilon) d\epsilon = \int_{E_p \geq \epsilon}^{\infty} j(E_p) p(\epsilon, E_p) \eta(E_p) dE_p d\epsilon \quad (1)$$

where ϵ and E_p are the energies of BSE and primary electrons, respectively, $p(\epsilon, E_p)$ is the probability function (PF) that describes the normalized BSE energy distribution produced by a monochromatic primary electron beam, that is, $\int_0^{\infty} p(\epsilon, E_p) d\epsilon = 1$, and $\eta(E_p)$ is the backscattering coefficient.

Discretizing Equation 1 over ϵ and E_p yields,

$$jj_k = \sum_{i \geq k} j_i \eta_i p_{k,i} \Delta E_i, \quad (2)$$

where jj_k is the k th element of the BSE flux ($k = 1, 2, \dots, n$) and η_i is the i th element of the discretized backscattering coefficient ($i = 1, 2, \dots, m$). Defining an $n \times m$ matrix \mathbf{A} as $A_{ki} = j_i p_{k,i} \Delta E_i$, we obtain a vectorized expression,

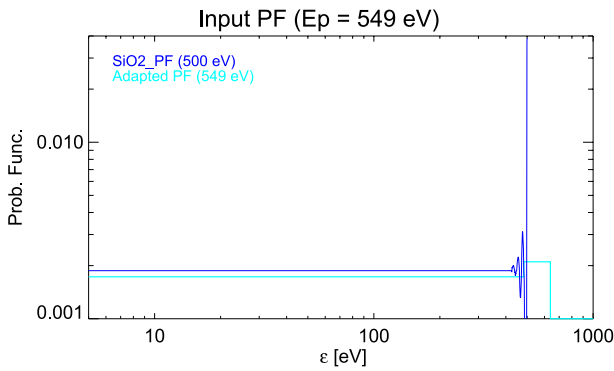


Figure 6. Probability functions (PFs) as a function of backscattered electrons energy ε for primary electrons with an energy of $E_p \sim 500$ eV. The blue thin line is the PF adopted from Dapor (2006), which is then averaged to Acceleration, Reconnection, Turbulence, and Electrodynamics of the Moon's Interaction with the Sun energy grids (the cyan line) for $E_p = 549$ eV (the closest energy channel).

$jj = \mathbf{A}\eta$, such that η can be determined by solving a standard matrix inversion problem:

$$\eta = \mathbf{A}^{-1}jj. \quad (3)$$

A similar procedure was successfully carried out for the determination of the photoemission yield based on ARTEMIS observations by Xu et al. (2021).

For selected BSE cases, jj and j are obtained from each ARTEMIS observation as described in the previous subsection. Note that when the Moon is immersed in the solar wind, the lunar surface potential (U_m) ranges from 0 to ~ 10 V on the sunlit hemisphere (e.g., Halekas et al., 2008, 2011b), which accelerates down-going SWE and decelerates upcoming BSE. These two processes are canceled out such that the fluxes measured by the spacecraft are mostly unaffected, though E_p could be corrected by adding U_m when solving Equation 3. Nevertheless, for the energy range of interest (50–600 eV), this effect is insignificant and thus ignored.

The last parameter necessary to solve for η is the probability function, $p(\varepsilon, E_p)$, which describes the probability that an incident electron with energy E_p is backscattered with an energy ε . In this study, we test different approaches

because the electron scattering behavior from laboratory experiments and modeling studies is not well characterized for lunar material. One of those is the PF from the simulations by Dapor (2006), and the other one is the analytical formalism by Staub (1994). The comparison of the two sets of PFs is provided in Figure S1. We have derived $\eta(E_p)$ based on both sets of PFs and the results are quite similar. Thus, we primarily show results with Dapor-PF and discuss the comparison toward the end.

In Figure 6, we show example simulation results of the BSE energy distribution produced by 500-eV primary electrons incident on silicon dioxide from Dapor (2006) (the blue line), including (a) an elastic backscattering peak at $\varepsilon = E_p$, (b) a constant value at $\varepsilon \leq \sim E_p - 80$ eV, and (c) peaks and troughs at $\varepsilon = [\sim E_p - 80, E_p]$ eV for inelastic scattering. For simplicity, in this study, we assume the probability function is applicable to all primary energies of interest and only preserve the elastic peak and ignore additional small-scale structures, consistent with the relatively coarse energy resolution of ARTEMIS data ($\Delta E/E = 0.32$). We preserve this energy resolution for both ε and E_p . The adapted PF for this study is thus comprised of a constant value for $0 < \varepsilon \leq E_p$ with an additional fraction, ζ , added to the energy grid at $\varepsilon = E_p$ for the elastic scattering contribution, more specifically,

$$p(\varepsilon, E_p) = \begin{cases} (1 - \zeta)/E_p & \text{for } 0 \leq \varepsilon \leq E_p - \Delta E_p \\ (1 - \zeta)/E_p + \zeta/\Delta E_p & \text{for } E_p - \Delta E_p \leq \varepsilon \leq E_p \end{cases} \quad (4)$$

A ζ of 0.05 is determined from the SiO₂ simulation results (Dapor, 2006) and applied to all E_p over 50–1,000 eV. In Figure 6, our adapted PF (“Dapor-PF”) at $E_p = 549$ eV with $\zeta = 0.05$ is shown as the cyan line.

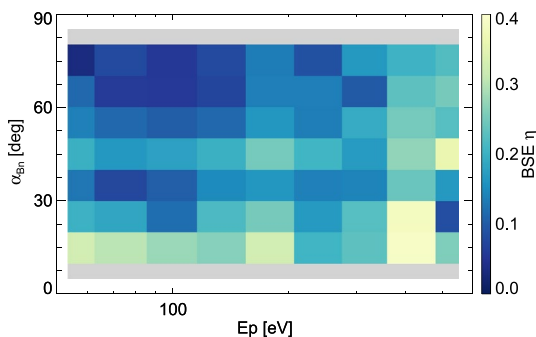


Figure 7. The calculated median η as a function of the primary electron energy E_p and the magnetic dip angle α_{Bn} .

3. Results

With the methodology described above, we derive the backscattering coefficient $\eta(E_p)$ for the selected 828 cases with a standard matrix inversion procedure, singular value decomposition, to solve the linear least squares problem (Xu et al., 2021). Figure 7 illustrates the calculated median η as a function of primary electron energy E_p and the magnetic dip angle α_{Bn} . Across all examined primary energies, η has a strong dependence on α_{Bn} , highest (0.3–0.4) at $\alpha_{Bn} = 0^\circ$ and lowest (0.1–0.2) at $\alpha_{Bn} = 75^\circ$. To illustrate this dependence further, Figure 8 shows η as a function of the magnetic dip angle α_{Bn} for $E_p = 132$ eV, which decreases from 0.3 to < 0.1 with increasing dip angle.

We interpret this dependence on the magnetic dip angle as an effect of a magnetized environment. Figure 9 illustrates the angular distributions of BSE

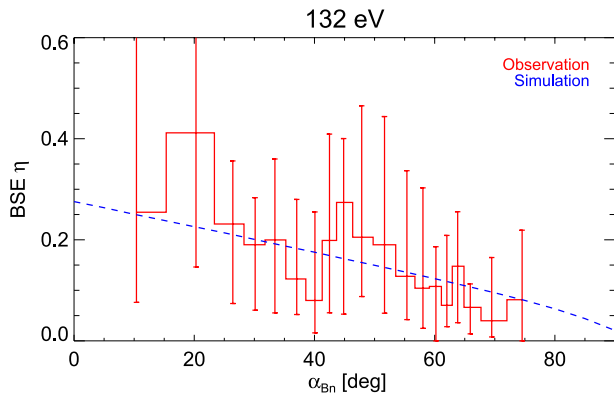


Figure 8. The BSE backscattering coefficient η as a function of the magnetic dip angle α_{Bn} for $E_p = 132$ eV, red for median values and quartiles as error bars and blue being the simulated curve (see text).

laboratory experiments or simulations). Meanwhile, these re-impacting BSEs in turn produce additional secondary electrons that may also contribute the surface current balance. It might be important to take into account this effect to accurately estimate the lunar surface charging.

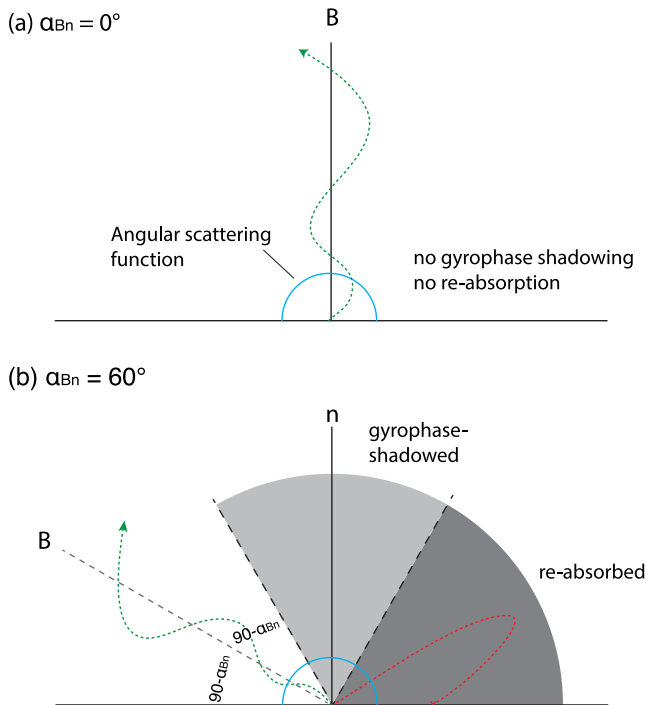


Figure 9. Schematics show the effects of a magnetized environment for different dip angles, (a) $\alpha_{Bn} = 0^\circ$ and (b) $\alpha_{Bn} = 60^\circ$. In (b), the dark gray area represents backscattered electrons with forward velocities along the magnetic field (pitch angles [PA] $> 90^\circ$) that will re-impact the surface. The light gray area represents a gyrophase-shadowing region of phase space, where BSEs within PA = $[90^\circ - \alpha_{Bn}, 90^\circ]$ may re-impact the surface, depending on their gyrophase. The red dashed curves show re-impacting electron trajectories for both scenarios and the green dashed curve shows BSEs that escape from the gyrophase-shadowing region of phase space. Finally, BSEs with PA $< 90^\circ - \alpha_{Bn}$ are free to travel back to the spacecraft.

(blue curves) at two dip angles, $\alpha_{Bn} = 0^\circ$ (Figure 9a) and 60° (Figure 9b). As shown in Figure 9b, the phase space of BSE is divided into three regions, dark gray for electron re-absorbing, light gray for gyrophase-shadowing, and white for free escaping. Gyrophase here refers to the angle between 0 and 2π that describes the orbit of the particle around the magnetic field under basic Larmor rotation. More specifically, considering a magnetic field pointing radially outward with $\alpha_{Bn} = 60^\circ$, those BSEs with PA $> 90^\circ$ have forward velocities and will return to the surface and get absorbed (red trajectory). The light gray highlights a phase space of $90^\circ - \alpha_{Bn} < PA < 90^\circ$, where some of the BSEs will also return to the surface (red trajectory) and those with the right initial gyrophases can escape back to the spacecraft (green trajectory), an effect called “gyrophase-shadowing” (Harada et al., 2013; Reiff, 1976). Finally, BSEs with PA $< 90^\circ - \alpha_{Bn}$ are free to travel back to the spacecraft with no absorption from the surface. In other words, for a magnetized environment like the lunar surface, depending on the magnetic dip angles, a significant portion of BSEs could be directed to re-impact the surface such that the total backscattering coefficient η could be significantly reduced compared to that in an unmagnetized environment (often the default setup for

We can simulate this effect with a simple particle tracing code and determine the fraction of BSE escaping for each dip angle, assuming an isotropic angular scattering. This simulated variation is overlaid as the blue dashed line in Figure 8 with a scaling factor of 0.28 (best fit with median values), which shows a good agreement with the observed variation (the red line).

Next, we examine the energy dependence of η . Figure 7 shows that η varies less with energy than α_{Bn} . Alternatively, the solid lines in Figure 10 are η as a function of primary electron energy E_p at different α_{Bn} . It shows that η is around 0.25–0.35 at $10^\circ < \alpha_{Bn} < 20^\circ$ and 0.10–0.20 at $50^\circ < \alpha_{Bn} < 60^\circ$ for the examined energy range (50–600 eV). It is worth noting that our derived η does not approach 0 at 50 eV like results from simulations and laboratory experiments (e.g., Demers et al., 2011; Nishimura et al., 1994), as we assume BSE goes down to 0 eV rather than cutting off at 50 eV, a more physical assumption.

In Figure 10, we also show results derived using alternative probability functions from Staub (1994) (as shown in Figure S1) for electrons with an incident angle of 0° (dotted lines) and 45° (dashed lines). Interestingly, while the “Dapor-PF” and “Staub-PF” are quite different, with the latter having a much less energy spread in BSE, the derived η are very similar to each other. This is perhaps a result of the relatively coarse energy resolution of the ARTEMIS measurements and/or the solar wind electron (primary electron) flux decreasing sharply with energy. That is, the derivation of η thus mainly depends on PFs at $\epsilon/E_p \sim 1$ and the difference in PFs at small ϵ/E_p is negligible. Ultimately, conclusions on the main characteristics of the observed behavior of the backscattering coefficient η remain the same for the different energy probability functions.

4. Discussion and Conclusions

When the Moon is immersed in the solar wind, the high-energy (>50 eV) tail of electrons emitted from the lunar surface consists of lunar photoelectrons (PHE) and BSE. In this study, we mainly utilize the oxygen Auger electron

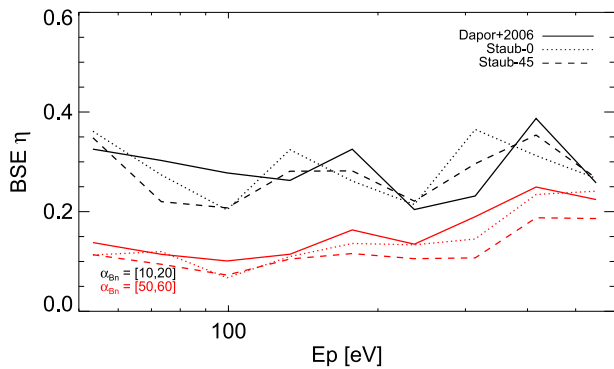


Figure 10. The BSE backscattering coefficient as a function of primary electron energy E_p at different α_{Bn} . The solid lines are derived based on the probability function (PF) shown in Figure 6 while the dotted and dashed lines use PFs from Staub (1994) for electrons with an incident angle of 0° and 45° , respectively.

peak feature in the lunar photoelectron energy spectrum to isolate cases of emitted electrons that are dominated by BSE over PHE. By adapting the BSE energy distribution for silicon dioxide provided by Dapor (2006) to be the probability function (PF) for lunar BSE, we derive the backscattering coefficient η with electron fluxes measured by ARTEMIS.

We have examined the dependence of η on the magnetic dip angle (α_{Bn}) and primary electron energy (E_p). η is found to have a strong dependence on α_{Bn} , most likely a result of a magnetized environment. As illustrated in Figure 9b, BSEs are magnetized to the IMF near the lunar surface and will re-impact the surface if they have forward velocities ($PA > 90^\circ$). Furthermore, those BSE with $PA = [90^\circ - \alpha_{Bn}, 90^\circ]$ can either return to the surface or escape back to space depending their initial gyrophase (gyrophase shadowing effect). Both effects reduce the overall flux of BSE emitted from the lunar surface, thus a reduced backscattering coefficient η . The variation of η with α_{Bn} inferred from data agrees well with a simple theoretical solution of this magnetization effect. Meanwhile, re-impacting BSE could backscatter again and escape or produce additional secondary electrons.

There is no obvious dependence of the derived η on the primary electron energy, ~ 0.3 within 50–600 eV. We have also tested other BSE energy distributions, which give similar results. This insensitivity to the choice of PF is probably because of a combination of the coarse energy resolution of the ARTEMIS data and the flux of solar wind electrons dropping sharply with energy. Thus, the derivation of η mainly depends on probability functions at $\epsilon/E_p \sim 1$ but is insensitive to discrepancies at small ϵ/E_p . Due to the dependence on the energy and the dip angle, the influence of electrons to the surface charging of the Moon (and any airless body) will depend on solar wind and IMF conditions, but also on the location on the surface.

In this study, we mainly use the high-photoemission-yield curve to remove the contamination from PHE. In Figure 11, we compare the derived BSE η based on the high-photoemission-yield curve (the red solid line) and the low-photoemission-yield curve (the blue solid line), limited to $\alpha_{Bn} < 20^\circ$. η mainly differs at lower energies (< 150 eV) by 0.1, at which the two yield curves also differ. Meanwhile, we do not expect secondary electrons produced by high-energy electrons and solar wind ions to significantly impact our results as the secondary electrons tend to be cold (a temperature of a few eV) and their fluxes are insignificant compared to PHE and BSE at the energy range examined here (e.g., Scholtz et al., 1996; Tsujita et al., 2004). We thus forgo the correction for secondary electrons in this study.

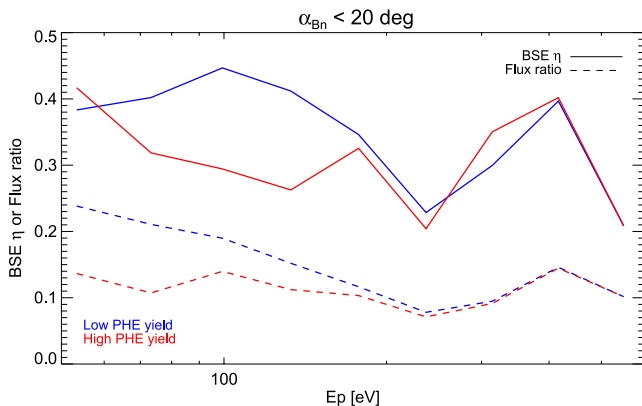


Figure 11. The BSE backscattering coefficient as a function of primary electron energy E_p at $\alpha_{Bn} < 20^\circ$ for the high-photoemission-yield curve (the red solid line) and the low-photoemission-yield curve (the blue solid line). The dashed red and blue lines are the flux ratios for the high-photoemission-yield case and the low-photoemission-yield case, respectively.

Finally, as the primary electron flux decreases with increasing energy, η should decrease with increasing contributions from the elastic backscattering and the lower limit of η can be inferred by assuming (unrealistically) pure elastic backscattering. This would be equivalent to calculating the ratio of upward and downward electron fluxes at the same energy. In Figure 11, we show the flux ratios for the high-photoemission-yield case and the low-photoemission-yield case as the dashed red and blue lines, respectively. The median flux ratio is around 0.1 for the high-photoemission-yield case but decreases from ~ 0.2 at 50 eV to ~ 0.1 at 600 eV for the low-photoemission-yield case. In other words, we can infer 0.1 within 50–600 eV as the lower limit of η . Note that the laboratory experiments or simulations mainly focus on characterizing η at hundreds of eV or keV. In contrast, our study characterizes η at the less explored lower energies, providing data-constrained results for the characterization of the lunar surface properties and to be compared with future laboratory experiments and simulations.

In summary, this study provides a methodology to differentiate two of the dominant lunar surface electron populations and thus a better understanding of the plasma environment near the lunar surface and helps the interpretation of the electron measurements by the upcoming Heliophysics Environmental and Radiation Measurement Experiment Suite mission. Our study also

motivates for future electron instrumentation with a better energy resolution to gain a better characterization of the lunar surface electrons. Moreover, we have calculated the electron backscattering coefficient of the lunar surface with ARTEMIS observations, which gives important insights into the properties of the lunar surface. Furthermore, the Moon experiences very different plasma environments as it orbits around Earth and our investigation of the backscattering coefficient can be applied to all these plasma conditions to better characterize the surface charging, also noting the importance of taking into account a magnetized environment. Last but not least, our technique of inferring the electron backscattering coefficient could potentially be applied to other airless bodies, such as Mercury, particularly with low-energy electron measurements as provided by BepiColombo.

Data Availability Statement

All ARTEMIS data necessary for this study are publicly available at <http://artemis.ssl.berkeley.edu>, including the EFI, ESA, and FGM data available at http://themis.ssl.berkeley.edu/data_products/. The results presented in this study rely on the FISM2 model described in Chamberlin et al. (2020). These data were accessed via the LASP Interactive Solar Irradiance Datacenter (LISIRD) <https://lasp.colorado.edu/lisird/>. Data access and processing was done using SPEDAS V3.1 (<http://spedas.org/wiki>), see Angelopoulos et al. (2019). The research data presented in this manuscript is included in the accompanying data set uploaded on Figshare (Xu et al., 2023).

Acknowledgments

S.X., A.R.P., and P. S. S. acknowledge support from NASA's Lunar Data Analysis Program, Grant 80NSSC18K1565. A.R.P., P. S. S., and J.S.H. also gratefully acknowledge support from NASA's Solar System Exploration Research Virtual Institute (SSERVI), Grants NNX14AG16A and NNX15AH15A. The ARTEMIS mission is funded and operated under NASA Grant NAS5-02099, and we specifically acknowledge C. W. Carlson and J. P. McFadden for use of ESA data, J. W. Bonnell and F. S. Mozer for use of EFI data, and K.-H. Glassmeier, U. Auster, and W. Baumjohann for the use of FGM data provided under the lead of the Technical University of Braunschweig and with financial support through the German Ministry for Economy and Technology and the German Center for Aviation and Space (DLR), Contract 50 OC 0302.

References

- Angelopoulos, V. (2009). *The THEMIS mission* (pp. 5–34). Springer.
- Angelopoulos, V. (2011). The ARTEMIS mission. *Space Science Reviews*, 165(1–4), 3–25. <https://doi.org/10.1007/s11214-010-9687-2>
- Angelopoulos, V., Cruce, P., Drozdov, A., Grimes, E., Hatzigeorgiu, N., King, D., et al. (2019). The Space Physics Environment Data Analysis System (SPEDAS). *Space Science Reviews*, 215(1), 9. <https://doi.org/10.1007/s11214-018-0576-4>
- Auster, H., Glassmeier, K., Magnes, W., Aydogar, O., Baumjohann, W., Constantinescu, D., et al. (2008). The THEMIS fluxgate magnetometer. *Space Science Reviews*, 141(1–4), 235–264. <https://doi.org/10.1007/s11214-008-9365-9>
- Bonnell, J., Mozer, F., Delory, G., Hull, A., Ergun, R., Cully, C., et al. (2009). The electric field instrument (EFI) for THEMIS. In *The THEMIS mission* (pp. 303–341). Springer.
- Borovsky, J. E., & Delzanno, G. L. (2021). Do impulsive solar-energetic-electron (SEE) events drive high-voltage charging events on the night-side of the moon? *Frontiers in Astronomy and Space Sciences*, 8, 655333. <https://doi.org/10.3389/fspas.2021.655333>
- Chamberlin, P. C., Eparvier, F. G., Knoer, V., Leise, H., Pankratz, A., Snow, M., et al. (2020). The flare irradiance spectral model-version 2 (FISM2). *Space Weather*, 18(12), e2020SW002588. <https://doi.org/10.1029/2020sw002588>
- Chamberlin, P. C., Woods, T. N., & Eparvier, F. G. (2007). Flare irradiance spectral model (FISM): Daily component algorithms and results. *Space Weather*, 5(7), 1–23. <https://doi.org/10.1029/2007sw000316>
- Chamberlin, P. C., Woods, T. N., & Eparvier, F. G. (2008). Flare irradiance spectral model (FISM): Flare component algorithms and results. *Space Weather*, 6(5), S05001. <https://doi.org/10.1029/2007sw000372>
- Collier, M. R., Newheart, A., Poppe, A. R., Hills, H. K., & Farrell, W. M. (2017). Stair-step particle flux spectra on the lunar surface: Evidence for nonmonotonic potentials? *Geophysical Research Letters*, 44(1), 79–87. <https://doi.org/10.1002/2016gl071457>
- Dapor, M. (2006). Energy loss spectra of low primary energy (E0? 1 keV) electrons backscattered by silicon dioxide. *Surface Science*, 600(20), 4728–4734. <https://doi.org/10.1016/j.susc.2006.07.043>
- De Hoffmann, F., & Teller, E. (1950). Magneto-hydrodynamic shocks. *Physical Review*, 80(4), 692–703. <https://doi.org/10.1103/PhysRev.80.692>
- Demers, H., Poirier-Demers, N., Couture, A. R., Joly, D., Guilmain, M., de Jonge, N., & Drouin, D. (2011). Three-dimensional electron microscopy simulation with the CASINO Monte Carlo software. *Scanning*, 33(3), 135–146. <https://doi.org/10.1002/sca.20262>
- Farrell, W., Stubbs, T., Delory, G., Vondrak, R., Collier, M., Halekas, J., & Lin, R. (2008). Concerning the dissipation of electrically charged objects in the shadowed lunar polar regions. *Geophysical Research Letters*, 35(19), L19104. <https://doi.org/10.1029/2008gl034785>
- Feuerbacher, B., Anderegg, M., Fitton, B., Laude, L., Willis, R., & Grard, R. (1972). Photoemission from lunar surface fines and the lunar photoelectron sheath. In *Lunar and planetary science conference proceedings* (Vol. 3, p. 2655).
- Halekas, J., Delory, G., Brain, D., Lin, R., Fillingim, M., Lee, C., et al. (2007). Extreme lunar surface charging during solar energetic particle events. *Geophysical Research Letters*, 34(2), L02111. <https://doi.org/10.1029/2006gl028517>
- Halekas, J., Delory, G., Farrell, W., Angelopoulos, V., McFadden, J., Bonnell, J., et al. (2011a). First remote measurements of lunar surface charging from ARTEMIS: Evidence for nonmonotonic sheath potentials above the dayside surface. *Journal of Geophysical Research*, 116(A7), A07103. <https://doi.org/10.1029/2011ja016542>
- Halekas, J., Delory, G., Lin, R., Stubbs, T., & Farrell, W. (2008). Lunar Prospector observations of the electrostatic potential of the lunar surface and its response to incident currents. *Journal of Geophysical Research*, 113(A9), A09102. <https://doi.org/10.1029/2008ja013194>
- Halekas, J., Delory, G., Lin, R., Stubbs, T., & Farrell, W. (2009a). Lunar prospector measurements of secondary electron emission from lunar regolith. *Planetary and Space Science*, 57(1), 78–82. <https://doi.org/10.1016/j.pss.2008.11.009>
- Halekas, J., Delory, G., Lin, R., Stubbs, T., & Farrell, W. (2009b). Lunar surface charging during solar energetic particle events: Measurement and prediction. *Journal of Geophysical Research*, 114(A5), A05110. <https://doi.org/10.1029/2009ja014113>
- Halekas, J., Mitchell, D., Lin, R., Hood, L., Acuña, M., & Binder, A. (2002). Evidence for negative charging of the lunar surface in shadow. *Geophysical Research Letters*, 29(10), 77–81. <https://doi.org/10.1029/2001gl014428>
- Halekas, J., Poppe, A., Delory, G., Farrell, W., & Horányi, M. (2012a). Solar wind electron interaction with the dayside lunar surface and crustal magnetic fields: Evidence for precursor effects. *Earth Planets and Space*, 64(2), 73–82. <https://doi.org/10.5047/eps.2011.03.008>
- Halekas, J., Poppe, A., Delory, G., Sarantos, M., Farrell, W., Angelopoulos, V., & McFadden, J. (2012b). Lunar pickup ions observed by ARTEMIS: Spatial and temporal distribution and constraints on species and source locations. *Journal of Geophysical Research*, 117(E6), E06006. <https://doi.org/10.1029/2012je004107>

- Halekas, J., Saito, Y., Delory, G., & Farrell, W. (2011b). New views of the lunar plasma environment. *Planetary and Space Science*, 59(14), 1681–1694. <https://doi.org/10.1016/j.pss.2010.08.011>
- Harada, Y., Machida, S., Halekas, J., Poppe, A. R., & McFadden, J. P. (2013). ARTEMIS observations of lunar dayside plasma in the terrestrial magnetotail lobe. *Journal of Geophysical Research: Space Physics*, 118(6), 3042–3054. <https://doi.org/10.1002/jgra.50296>
- Harada, Y., Poppe, A. R., Halekas, J. S., Chamberlin, P. C., & McFadden, J. P. (2017). Photoemission and electrostatic potentials on the dayside lunar surface in the terrestrial magnetotail lobes. *Geophysical Research Letters*, 44(11), 5276–5282. <https://doi.org/10.1002/2017GL073419>
- Jarvinen, R., Alho, M., Kallio, E., Wurz, P., Barabash, S., & Futaana, Y. (2014). On vertical electric fields at lunar magnetic anomalies. *Geophysical Research Letters*, 41(7), 2243–2249. <https://doi.org/10.1002/2014gl059788>
- Kallio, E., Jarvinen, R., Dyadechkin, S., Wurz, P., Barabash, S., Alvarez, F., et al. (2012). Kinetic simulations of finite gyroradius effects in the lunar plasma environment on global, meso, and microscales. *Planetary and Space Science*, 74(1), 146–155. <https://doi.org/10.1016/j.pss.2012.09.012>
- Kato, M., Harada, Y., Xu, S., Poppe, A. R., Halekas, J. S., Miyake, Y., et al. (2023). Modeling photoelectron and auger electron emission from the sunlit lunar surface: A comparison with ARTEMIS observations. *Journal of Geophysical Research: Space Physics*, 128(10), e2023JA031707. <https://doi.org/10.1029/2023JA031707>
- Manka, R. H. (1973). Plasma and potential at the lunar surface. In *Photon and particle interactions with surfaces in space* (pp. 347–361). Springer.
- McFadden, J., Carlson, C., Larson, D., Ludlam, M., Abiad, R., Elliott, B., et al. (2008). The THEMIS ESA plasma instrument and in-flight calibration. *Space Science Reviews*, 141(1–4), 277–302. <https://doi.org/10.1007/s11214-008-9440-2>
- Mitchell, D., Halekas, J., Lin, R., Frey, S., Hood, L., Acuña, M., & Binder, A. (2008). Global mapping of lunar crustal magnetic fields by Lunar Prospector. *Icarus*, 194(2), 401–409. <https://doi.org/10.1016/j.icarus.2007.10.027>
- Nishimura, K., Itotani, T., & Ohya, K. (1994). Influence of surface roughness on secondary electron emission and electron backscattering from metal surface. *Japanese Journal of Applied Physics*, 33(8R), 4727. <https://doi.org/10.1143/jjap.33.4727>
- Nitter, T., Havnes, O., & Melandsø, F. (1998). Levitation and dynamics of charged dust in the photoelectron sheath above surfaces in space. *Journal of Geophysical Research*, 103(A4), 6605–6620. <https://doi.org/10.1029/97ja03523>
- Pedersen, A. (1995). Solar wind and magnetosphere plasma diagnostics by spacecraft electrostatic potential measurements. In *Annales geophysicae* (Vol. 13, pp. 118–129).
- Poppe, A., Halekas, J., Samad, R., Sarantos, M., & Delory, G. (2013). Model-based constraints on the lunar exosphere derived from ARTEMIS pickup ion observations in the terrestrial magnetotail. *Journal of Geophysical Research: Planets*, 118(5), 1135–1147. <https://doi.org/10.1002/jgre.20090>
- Poppe, A., Halekas, J. S., & Horányi, M. (2011). Negative potentials above the day-side lunar surface in the terrestrial plasma sheet: Evidence of non-monotonic potentials. *Geophysical Research Letters*, 38(2), L02103. <https://doi.org/10.1029/2010gl046119>
- Poppe, A., & Horányi, M. (2010). Simulations of the photoelectron sheath and dust levitation on the lunar surface. *Journal of Geophysical Research*, 115(A8), A08106. <https://doi.org/10.1029/2010ja015286>
- Poppe, A., Samad, R., Halekas, J., Sarantos, M., Delory, G., Farrell, W., et al. (2012). ARTEMIS observations of lunar pick-up ions in the terrestrial magnetotail lobes. *Geophysical Research Letters*, 39(17), L17104. <https://doi.org/10.1029/2012gl052909>
- Poppe, A. R., Halekas, J. S., Delory, G. T., Farrell, W. M., Angelopoulos, V., McFadden, J. P., et al. (2012). A comparison of ARTEMIS observations and particle-in-cell modeling of the lunar photoelectron sheath in the terrestrial magnetotail. *Geophysical Research Letters*, 39(1), L01102. <https://doi.org/10.1029/2011GL050321>
- Reiff, P. H. (1976). Magnetic shadowing of charged particles by an extended surface. *Journal of Geophysical Research*, 81(19), 3423–3427. <https://doi.org/10.1029/ja081i019p03423>
- Scholtz, J., Dijkamp, D., & Schmitz, R. (1996). Secondary electron emission properties. *Philips Journal of Research*, 50(3–4), 375–389. [https://doi.org/10.1016/s0165-5817\(97\)84681-5](https://doi.org/10.1016/s0165-5817(97)84681-5)
- Schreiber, E., & Fitting, H.-J. (2002). Monte Carlo simulation of secondary electron emission from the insulator SiO₂. *Journal of Electron Spectroscopy and Related Phenomena*, 124(1), 25–37. [https://doi.org/10.1016/s0368-2048\(01\)00368-1](https://doi.org/10.1016/s0368-2048(01)00368-1)
- Schwan, J., Wang, X., Hsu, H.-W., Grün, E., & Horny, M. (2017). The charge state of electrostatically transported dust on regolith surfaces. *Geophysical Research Letters*, 44(7), 3059–3065. <https://doi.org/10.1002/2017GL072909>
- Staub, P.-F. (1994). Bulk target backscattering coefficient and energy distribution of 0.5–100 keV electrons: An empirical and synthetic study. *Journal of Physics D: Applied Physics*, 27(7), 1533–1537. <https://doi.org/10.1088/0022-3727/27/7/030>
- Sternovsky, Z., Chamberlin, P., Horányi, M., Robertson, S., & Wang, X. (2008). Variability of the lunar photoelectron sheath and dust mobility due to solar activity. *Journal of Geophysical Research*, 113(A10), A10104. <https://doi.org/10.1029/2008ja013487>
- Szabo, P. S., Poppe, A. R., Biber, H., Mutzke, A., Pichler, J., Jäggi, N., et al. (2022). Deducing lunar regolith porosity from energetic neutral atom emission. *Geophysical Research Letters*, 49(21), e2022GL101232. <https://doi.org/10.1029/2022GL101232>
- Thomas, S., & Pattinson, E. (1970). Range of electrons and contribution of back-scattered electrons in secondary production in aluminium. *Journal of Physics D: Applied Physics*, 3(3), 349–357. <https://doi.org/10.1088/0022-3727/3/3/315>
- Tsujita, T., Nagatomi, T., Takai, Y., Morita, Y., Nishitani, M., Kitagawa, M., & Uenoyama, T. (2004). Energy distribution of ion-induced secondary electrons from MGO surface. *Japanese Journal of Applied Physics*, 43(6B), L753. <https://doi.org/10.1143/jjap.43.L753>
- Vorburger, A., Wurz, P., Barabash, S., Wieser, M., Futaana, Y., Lue, C., et al. (2013). Energetic neutral atom imaging of the lunar surface. *Journal of Geophysical Research: Space Physics*, 118(7), 3937–3945. <https://doi.org/10.1002/jgra.50337>
- Wang, X., Schwan, J., Hsu, H.-W., Grün, E., & Horny, M. (2016). Dust charging and transport on airless planetary bodies. *Geophysical Research Letters*, 43(12), 6103–6110. <https://doi.org/10.1002/2016GL069491>
- Whipple, E. C. (1981). Potentials of surfaces in space. *Reports on Progress in Physics*, 44(11), 1197–1250. <https://doi.org/10.1088/0034-4885/44/11/002>
- Xu, S., Liemohn, M., Bougher, S., & Mitchell, D. (2015). Enhanced carbon dioxide causing the dust storm-related increase in high-altitude photoelectron fluxes at Mars. *Geophysical Research Letters*, 42(22), 9702–9710. <https://doi.org/10.1002/2015gl066043>
- Xu, S., & Liemohn, M. W. (2015). Superthermal electron transport model for Mars. *Earth and Space Science*, 2(3), 47–64. <https://doi.org/10.1002/2014EA000043>
- Xu, S., Poppe, A. A., Szabo, P. S., Harada, Y., Halekas, J. S., & Chamberlin, P. (2023). Characteristics of lunar surface electrons inferred from ARTEMIS observations I: Backscattered electrons [Dataset]. <https://doi.org/10.6084/m9.figshare.24223444.v1>
- Xu, S., Poppe, A. R., Halekas, J. S., & Harada, Y. (2020). Reflected protons in the lunar wake and their effects on wake potentials. *Journal of Geophysical Research: Space Physics*, 125(7), e2020JA028154. <https://doi.org/10.1029/2020ja028154>
- Xu, S., Poppe, A. R., Halekas, J. S., Mitchell, D. L., McFadden, J. P., & Harada, Y. (2019). Mapping the lunar wake potential structure with ARTEMIS data. *Journal of Geophysical Research: Space Physics*, 124(5), 3360–3377. <https://doi.org/10.1029/2019JA026536>

- Xu, S., Poppe, A. R., Harada, Y., Halekas, J. S., & Chamberlin, P. C. (2021). Lunar photoemission yields inferred from ARTEMIS measurements. *Journal of Geophysical Research: Planets*, 126(6), e2020JE006790. <https://doi.org/10.1029/2020je006790>
- Yokota, S., Saito, Y., Asamura, K., Tanaka, T., Nishino, M. N., Tsunakawa, H., et al. (2009). First direct detection of ions originating from the moon by MAP-PACE IMA onboard SELENE (KAGUYA). *Geophysical Research Letters*, 36(11), L11201. <https://doi.org/10.1029/2009gl038185>